Communication

In Situ Observation of Phase Transformations in the Coarse-Grained Heat-Affected Zone of P91 Heat-Resistant Steel During Simulated Welding Process

YANG SHEN, BO CHEN, and CONG WANG

The solid-state phase transformation in the coarse-grained heat-affected zone of P91 steel under simulated welding thermal cycle has been investigated *in situ* by confocal scanning laser microscope. It is found that γ-austenite initiates from the triple point of δ-ferrite grain boundaries (GBs), then at ordinary δ-GBs, and eventually from grain interiors. Upon further cooling, martensite laths are observed to nucleate and growth instantaneously, with the growth rate being estimated ranging from 175 to 454 μm/s.

It is well established that the coarse-grained heat-affected zone (CGHAZ) of the welded joints could form heterogeneous microstructures after welding, such as retained δ-ferrite, retained γ-austenite, and martensite, which to a large extent dictate the mechanical properties of the welded joints.[1] In addition, reheat cracks and type III creep cracks may occur in the CGHAZ, which deteriorate the creep rupture strength of the heat-resistant pressure vessel components.[2–4] The as-weld microstructure in the CGHAZ has been shown to be responsible for the subsequent structural evolution during post-weld heat treatment as well as in service at high temperatures.[5] Consequently, it is important to elucidate the phase transformation and microstructure evolution in the CGHAZ during the welding thermal cycle.

YANG SHEN and CONG WANG are with the School of Metallurgy, Northeastern University, Shenyang 110819, China. Contact e-mail: wangc@smm.neu.edu.cn BO CHEN is with the School of Engineering, University of Leicester, Leicester LE1 7RH, UK.

Previous CGHAZ studies were primarily based on post-mortem examinations performed at ambient temperature and/or mathematical calculations. Sawada *et al.*[6] systematically investigated the nonequilibrium microstructure of the heat-affected zone (HAZ) in the as-welded P91 steel and revealed that the CGHAZ exhibited the highest hardness because of the martensite structure with fine laths and high dislocation density. Ueshima *et al.*[7,8] by means of mathematical analysis, focused on the redistribution of solutes at δ/γ interfaces during solidification. However, experimental evidence remains scarce pertinent to phase transformations and microstructural evolution during continuous heating and cooling typical of welding. Such information will certainly enrich our understanding of the kinetics of microstructural evolution during welding and enable developing a comprehensive computational model for CGHAZ.

One of the powerful *in situ* approaches to investigate phase transformations and microstructural evolution in steels is high-temperature confocal scanning laser microscopy (CSLM), which breaks the predicament of traditional metallographic experiments and is capable of tracking real-time morphology and performing quantitative analysis.[9–11] Zou *et al.*[12] utilized CSLM for *in situ* observations of ferrite laths growth behaviors in the HAZ and found that the increase of cooling rate was beneficial to the formation of acicular ferrites instead of ferrite side plates. Dippenaar *et al.*[13] observed the development of δ-ferrite recovery substructure in low carbon steels though CSLM. It was proposed that the sub-boundary structures in δ-ferrite could play a role in modifying austenite decomposition products. CSLM can provide real-time observations, which are not readily available by *in situ* time-resolved X-ray diffraction using high-energy synchrotron radiation (HEXRD), as the latter technique can only present lattice parameter and other peak information (i.e. an indirect microstructural observation).[10,14] In this respect, CSLM is a complimentary tool to HEXRD in terms of revealing the phase transformation process. Furthermore, with the accessibility of electron backscatter diffraction (EBSD) technique, grain orientations and local strain distributions of the CGHAZ can be quantitatively analyzed.[15,16]

The purpose of the present work is to, through a simulated welding thermal cycle, document possible phase transformations and quantify kinetic processes involving martensite growth by *in situ* CSLM observation, which will be coupled by *ex situ* crystallographic features enabled by EBSD. It is anticipated that a sophisticated understanding of the morphology and crystallography of the CGHAZ will bode well to fine tune the mechanical properties and serve as an accurate prediction of creep behavior of the weldment.

P91 steel (ASTM A335) with 273 mm outer diameter and 25.4 mm wall thickness was used as the target

material. It was normalized at 1333 K for 30 minutes and tempered at 1033 K for 60 minutes. The chemical composition of the adopted steel is shown in Table I.

A CSLM (VL2000DX-SVF18SP, Yonekura Manufacturing Corporation, Japan) with a purple laser diode (wavelength of 405 nm) was employed for *in situ* observation. The sample was machined into a disc with the dimension of Φ 5 × 4 mm. Then, the specimen was mechanically ground, mirror polished, positioned in an alumina crucible, and immediately subjected to the following thermal cycle: (1) heating to 473 K at a rate of 40 K/min, holding for 30 seconds, (2) heating to 1673 K ($T_p \gg Ac_3 = 1165$K) at 1000 K/min, holding for 20 seconds, (3) continuously cooling to room temperature at programmed cooling rate under high-purity argon in the furnace, as shown in Figure 1.[17] This thermal cycle was designed for simulating the thermal cycle of the CGHAZ adjacent to the weld fusion line in shielded metal arc welding (SMAW) process with 18 kJ/cm heat input. During cooling, successive images were recorded at a rate of 15 frames per second and collected by a charge-couple device (CCD) camera.

The specimen after *in situ* observation was prepared by standard metallographic procedures. The crystallographic features were revealed by a field-emission scanning electron microscope (FESEM, MAIA3 XMH, TESCAN, CZ) operating at 20 kV, which is coupled with an EBSD with the sample stage being tilted by 70 deg and fitted with a NordlysMax³ detector (Oxford Instruments) and HKL CHANNEL5 software. More detailed description of preparing EBSD specimen was presented elsewhere.[18,19] Nanoindentation testing of the CGHAZ was performed on a polished surface at room temperature using a nano-mechanical tester (G200, KLA, USA), and at least 20 indentations were obtained to ensure repeatability.

Figure 2 shows typical CSLM snapshots of δ-ferrite to γ-austenite and to martensite phase transformations observed *in situ*. After holding at the peak temperature where single-phase δ-ferrite prevails, the migration of δ-ferrite grain boundary (δ-GB) could be noticed during the subsequent cooling process, whose orientations and traces are labeled by white arrows and white dash lines in Figure 2(a), respectively. Moreover, once the δ-GB movement stops, GB grooves become deeper and clearer because the interfacial tension is directed inwardly against the bulk sample.[9] As shown by the red dotted squares in Figure 2(b), the appearance of the γ-austenite phase in the δ-ferrite matrix at the very beginning of the δ-ferrite to γ-austenite transformation is usually observed first from the triple point of the δ-GBs with a trihedral shape, represented by the γ_1-cell in the inset of Figure 2(b), on the sample surface at 1468 K. Subsequently, the second γ-austenite cell (γ_2-cell), as shown by the green dotted squares in Figure 2(c), forms

at the δ-GBs with a dihedral shape, which is observed at 1348 K. Upon further cooling, as displayed by the red and green dotted squares in the inset of Figures 2(c) and (d), γ_1-cell and γ_2-cell gradually spread along the δ-GBs and form a thin layer on both sides of the original δ-GBs. Afterwards, these γ-austenite cells grow into the δ-ferrite matrix, initially with a curved front, then exhibiting a finger-like pattern. Finally, the third γ-austenite cell (γ_3-cell), as shown by the blue dotted squares in Figure 2(d), forms in the δ-ferrite matrix with a spherical shape at 1201 K. After that, these γ-austenite cells spread and cover the entire δ-ferrite. Some GBs, which are not very obvious in the CSLM, may be the traces left by the γ-austenite GBs movement. As GBs of δ-ferrite and γ-austenite are sketched out in Figure 2(e), the average grain sizes of the δ-ferrite and γ-austenite are calculated to be 61.43 and 36.86 μm, respectively, by the line intercept method (ASTM E112) using Image J software.[20]

Following the above-mentioned δ-ferrite to γ-austenite phase transformation, another γ-austenite to martensite phase transformation processes are captured by CSLM observations, as shown in Figures 2(f) through (j). As shown by the cyan, yellow, and magenta circles in Figure 2(f), the initial martensite phase transformation occurs at 578 K according to the apparent surface relief by the displacive motion from austenite to martensite.[21–23] It can be clearly seen that the two martensite laths (M_1 and M_2) grow inside the grain and the other martensite lath (M_3) crosses the sub-grain boundary. With the decrease of temperature, as displayed by the green, blue, and red circles (M_4, M_5, and M_6) in Figures 2(g) through (i), the martensite lath growth occurs inside the grain. With the transformation progresses, martensite laths grow radially in the interior of γ-austenite grain and could cover the whole γ-austenite, and the finishing temperature of martensite phase transformation based on the last registered CSLM observation, Figure 2(j), was 541 K.

Moreover, detailed measurements of the growth rates from the six martensite laths are shown in Figure 2(k), which were measured from CSLM successive images using the Image J software. It is found that the first three martensite laths (M_1, M_2, and M_3) grow at the rate of 175, 181, and 149 μm/s, respectively. The slower growth rate of M_3 can be attributed to the obstruction by the sub-grain boundary.[24] One the other hand, the growth rates of M_4 (212 μm/s), M_5 (272 μm/s), and M_6 (454 μm/s) sharply increase, and the main reason responsible for the vast growth rate difference is probably dictated by the driving force for martensitic transformation, which is caused by the degree of supercooling as analyzed in previous work.[17] As for the error in result analysis, it can be attributed to the measurement (about 5 to 10 pct, verified by repeated tests) and the temperature difference

Table I.   Chemical Composition of P91 Steel (Weight Percent)

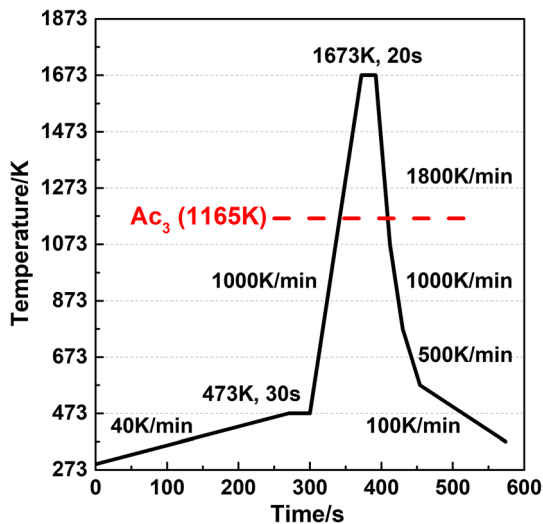| C	Mn	P	S	Si	Cr	Mo	V	N	Ni	Al	Nb
0.10	0.45	0.017	0.005	0.3	8.15	0.95	0.21	0.044	0.17	0.013	0.06

Fig. 1—Thermal cycle employed for *in situ* observation under CSLM (Color figure online).

between the sample surface and the bottom of the crucible (about 20 K to 40 K, depending on the sample material, thickness, and heating or cooling rate).[25]

The CSLM revealed that phase transformation processes during continuous cooling are consistent with the description by Yin *et al.*[9,26] and Phelan *et al.*[13,27] In addition, Morito *et al.*[28] and Yu *et al.*[29] demonstrated that martensite packet size and blocky width play an important role with respect to the strengthening of martensitic steels. The kinetic growth of different individual martensite laths could also lend strong support to optimize the welding parameters of this material, and potentially predict the creep behavior of the weldment during subsequent service.

Detailed crystallographic characteristics of the CGHAZ after simulated welding cycle by EBSD are presented in Figure 3. Band contrast distribution of the Kikuchi in Figure 3(a) shows a typical martensitic lath microstructure within the prior austenite grains (PAGs). The crystal orientation of martensite laths varies as displayed in the inverse pole figure (Figure 3(b)). The laths within individual martensite blocks represented by similar colors indicate that the martensite laths appearing in the same blocks tend to have a lower misorientation, while those from different blocks are segmented by higher misorientation. Local misorientation maps were processed to evaluate and visualize the plastic strain or deformation within grains by calculating kernel average misorientation (KAM) between groups of pixels/kernels within the grains.[16,30] KAM value with 1.35 deg in Figure 3(c) shows the high local strain energy levels or crystal deformations of the grains, suggesting the high degree of martensitic transformation in the CGHAZ. Grain boundary map in Figure 3(d) illustrates the multiple boundary structures. The boundaries between the martensite packets and blocks are identified as the high-angle grain boundaries (HAGBs, misorientation $\theta > 10$ deg) with red lines. The sub-

boundaries within the martensite blocks are mostly low-angle grain boundaries (LAGBs, misorientation $\theta < 10$ deg) denoted by blue lines, such as fine lath martensite boundaries. Normalized frequency of HAGBs is 46.8 pct, while that of LAGBs is 53.2 pct.

Statistical distribution of the misorientation angles between neighboring grains is shown in Figure 3(e). A bimodal-type distribution was found with the peak appearing at low (smaller than 10 deg) and high angles (from 58 to 62 deg). Various studies have confirmed that the bimodal grain boundary distribution may be conducive to form high strength and ductile metallic materials. The fine martensite with a high density of dislocations provide strength, while coarse martensite packets enable strain hardening and hence adequate ductility.[31–33] It is also widely recognized that the high misorientation boundaries are capable of arresting crack propagation, thus enhancing impact toughness.[34,35] Simultaneously, by nanoindentation, the hardness and Young's modulus of the CGHAZ are evaluated to be 6.6 $\pm$ 0.5 GPa and 263.7 $\pm$ 7.5 GPa, respectively, which are higher than those of the base metal (4.2 $\pm$ 0.4 GPa and 240.0 $\pm$ 11.8 GPa). The increased nanoindentation-determined hardness and Young's modulus in the CGHAZ are presumably due to the martensitic structure within the coarse PAGs and high dislocation density.[36,37]

Based on the observation and discussion above, an overview of phase transformations that occur in the CGHAZ of P91 steel is schematically illustrated in Figure 4. As the temperature cools down from 1673 K (the peak temperature of CGHAZ) to 1468 K, single-phase δ-ferrite continuously coarsens with a polygonal shape, as shown in Figure 4(a). With further temperature decreasing, γ-austenite preferentially nucleates on the triple points of the δ-GBs with a trihedral shape, indicated by the black arrow in Figure 4(b). Then, the γ-austenite grows along the δ-GBs with a dihedral shape, as shown in Figure 4(c). In this continuous cooling process, γ-austenite cells grow into the δ-ferrite matrix, first with a curved front, then with the finger-like pattern, as shown in Figure 4(d). At the same time, the third γ-austenite nucleates inside the δ-ferrite grain with a spherical shape. Finally, these γ-austenite cells gradually grow and merge together. After the temperature drops below 1063 K, austenitization is complete. The coarsening of γ-austenite grains is accompanied with the temperature reduction, and the final grain size is half that of the δ-ferrite, as shown in Figure 4(e). From 578 K (M_s) to 541 K (M_f), martensitic transformation starts. The growth rate of martensite lath sharply increases with decreasing temperature, as shown in Figures 4(f) and (g), which could be attributed to the degree of supercooling.[17] The developed martensitic microstructure exhibits hierarchical features such as packets and blocks, as schematically shown in Figure 4(h). It is observed that a single packet (indicated by the green dash lines in Figure 4(h)) consists of several blocks with different orientations. Each block (indicated by the black dash lines in Figure 4(h)) consists of laths with nearly the same orientations, which are misoriented by small angles of about 2 to 10 deg.
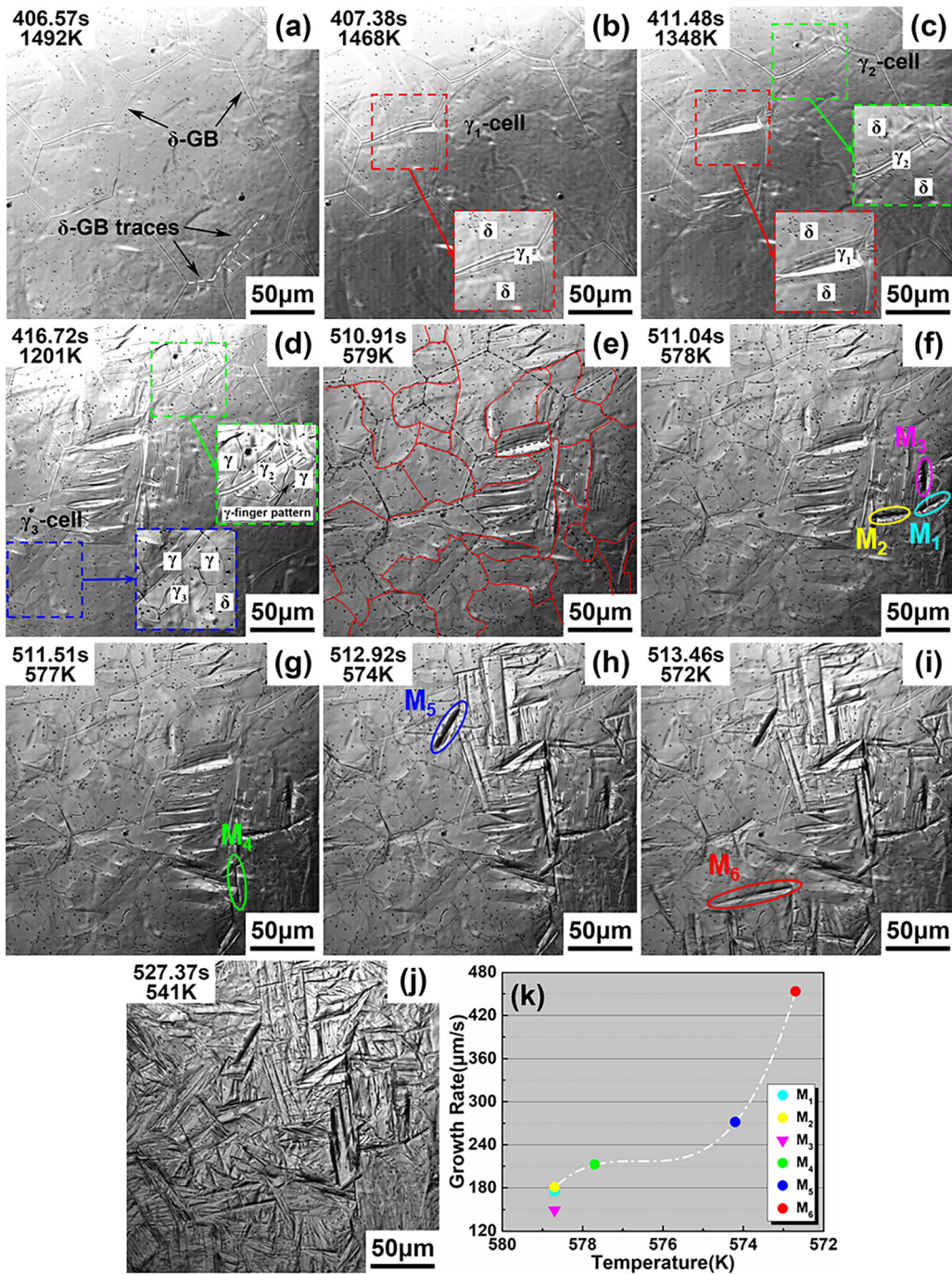
Fig. 2—(*a* through *e*) CSLM snapshots tracking the continuous morphological evolution of the δ-ferrite $\rightarrow$ γ-austenite phase transformation; (*f* through *j*) CSLM snapshots tracking the martensite growth during γ-austenite $\rightarrow$ martensite transformation process; (k) the relationship between growth rate against temperature for the six martensite laths. (Red, green, and blue dotted squares show the three γ-austenite nucleation sites, respectively; the grain boundaries of δ-ferrite and γ-austenite are indicated by the black dash lines and red solid lines, respectively; M_1, M_2, M_3, M_4, M_5, and M_6 represent the martensite laths.) (Color figure online).

In summary, a combined *in situ* CSLM observation with post-mortem EBSD crystallography characterization was performed to improve the understanding of phase transformation processes within the CGHAZ of a ferritic-martensitic steel subjected to a simulated welding process. Concluding remarks can be drawn:

1. Upon cooling, δ-ferrite to γ-austenite transformation takes place first. It is revealed that γ-cells
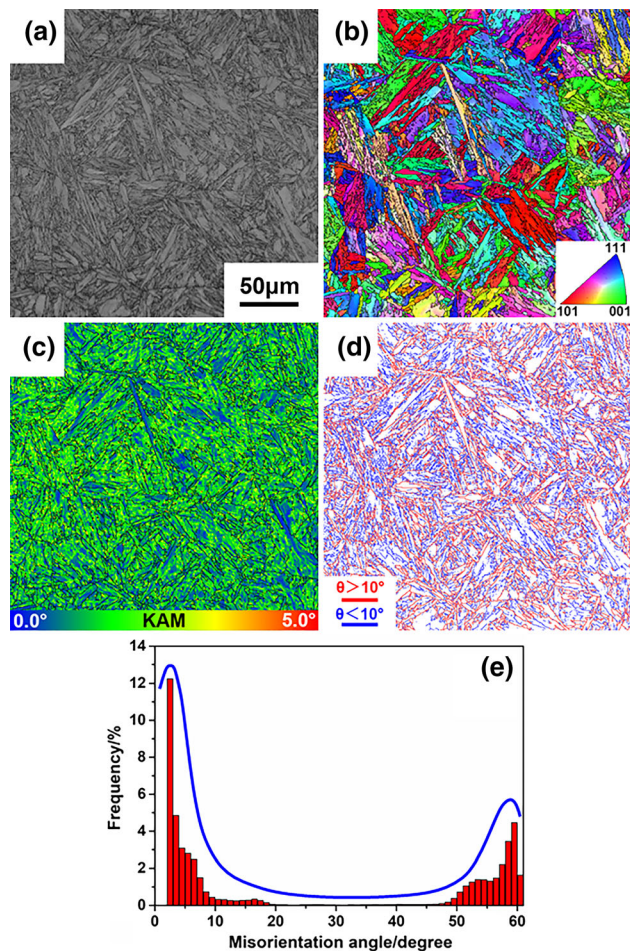
Fig. 3—EBSD analysis of the CGHAZ: (a) band contrast map; (b) inverse pole figure; (c) kernel average misorientation map; (d) grain boundary map; and (e) distribution histogram of misorientation angle (Color figure online).

preferentially nucleate at triple junctions of δ-GBs with trihedral shapes. Subsequently, γ-austenite may also find suitable nucleation sites along δ-GBs and grain interiors, but their morphologies change from dihedral to spherical.

2. Following austenitization, martensite laths grow rapidly in the interior of γ-austenite grains. The kinetics of the martensitic transformation shows a significant variation, increasing from 175 to 454 μm/s as the temperature decreases.

3. The higher misorientation boundaries (misorientation $\theta > 10$ deg) and the bimodal distribution of the martensite lath misorientation angles in the CGHAZ are believed to potentially enhance toughness and strength of the CGHAZ.
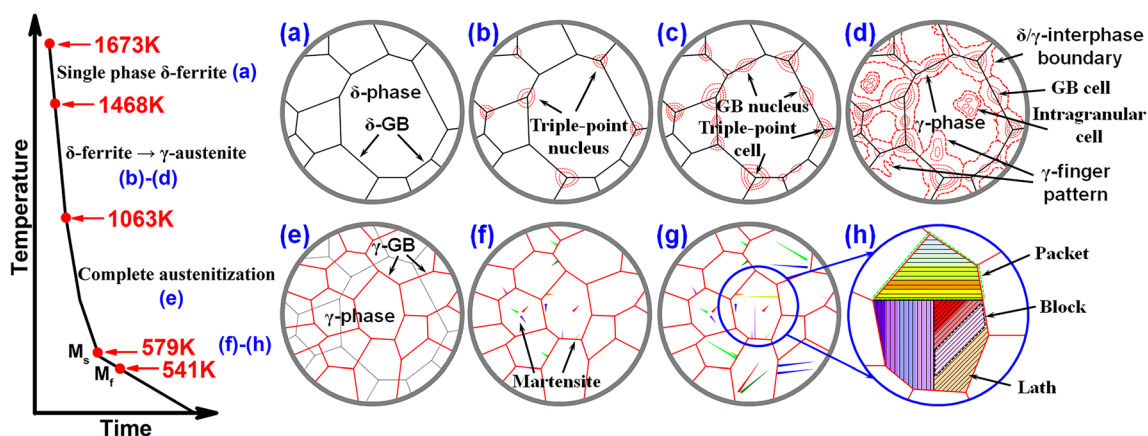
Fig. 4—Schematic illustrations of the phase transformation in the CGHAZ of P91 steel under typical welding thermal cycle: (a) single δ-ferrite; (b through d) δ-ferrite → γ-austenite phase transformation; (e) complete austenitization; (f through h) γ-austenite → martensite phase transformation (Color figure online).

REFERENCES

1. Y. Wang, R. Kannan, L. Zhang, and L. Li: *Weld. J.*, 2017, vol. 96, pp. 203–19.
2. K. Sedman, J. Thornley, and R. Griffin: *Eng. Fail. Anal.*, 1997, vol. 4, pp. 89–98.
3. S. Tavares, J. Pardal, G. Souza, P. Garcia, E. Barbosa, C. Barbosa, and I. CardoteFilho: *Eng. Fail. Anal.*, 2015, vol. 56, pp. 464–73.
4. J.A. Francis, W. Mazur, and H.K.D.H. Bhadeshia: *Mater. Sci. Technol.*, 2006, vol. 22, pp. 1387–95.
5. Y. Wang, R. Kannan, and L. Li: *Mater. Charact.*, 2016, vol. 118, pp. 225–34.
6. K. Sawada, T. Hara, M. Tabuchi, K. Kimura, and K. Kubushiro: *Mater. Charact.*, 2015, vol. 101, pp. 106–13.
7. Y. Ueshima, S. Mizoguchi, T. Matsumiya, and H. Kajioka: *Metall. Trans. B*, 1986, vol. 17, pp. 845–59.
8. Y. Ueshima, Y. Sawada, S. Mizoguchi, and H. Kajioka: *Metall. Trans. A*, 1989, vol. 20A, pp. 1375–83.
9. H. Yin, T. Emi, and H. Shibata: *Acta Mater.*, 1999, vol. 47, pp. 1523–35.
10. X. Yu, S.S. Babu, J.C. Lippold, H. Terasaki, and Y.I. Komizo: *Metall. Mater. Trans. A*, 2012, vol. 43, pp. 1538–46.
11. G. Mao, R. Cao, X. Guo, Y. Jiang, and J. Chen: *Metall. Mater. Trans. A*, 2017, vol. 48A, pp. 5783–98.
12. X. Zou, J. Sun, H. Matsuura, and C. Wang: *Metall. Mater. Trans. B*, 2018, vol. 49B, pp. 2168–73.
13. R.J. Dippenaar and D.J. Phelan: *Metall. Mater. Trans. B*, 2003, vol. 34B, pp. 495–501.
14. P. Mayr, T.A. Palmer, J.W. Elmer, E.D. Specht, and S.M. Allen: *Metall. Mater. Trans. A*, 2010, vol. 41A, pp. 2462–65.
15. F.J. Humphreys: *J. Mater. Sci.*, 2001, vol. 36, pp. 3833–54.
16. S.I. Wright, M.M. Nowell, and D.P. Field: *Microsc. Microanal.*, 2011, vol. 17, pp. 316–29.
17. Y. Shen and C. Wang: *Metall. Mater. Trans. A*, 2019, vol. 50A, pp. 4955–60.
18. Y. Shen and C. Wang: *Metall. Mater. Trans. B*, 2019, vol. 50B, pp. 595–600.
19. Y. Shen, J. Leng, and C. Wang: *J. Mater. Sci. Technol.*, 2019, vol. 35, pp. 1747–52.
20. C.A. Schneider, W.S. Rasband, and K.W. Eliceiri: *Nat. Methods*, 2012, vol. 9, pp. 671–75.
21. H. Bhadeshia and R. Honeycombe: *Steels: Microstructure and Properties*, 3rd ed., Butterworth-Heinemann, Oxford, 2017, pp. 95–112.
22. G. Miyamoto, N. Takayama, and T. Furuhara: *Scripta Mater.*, 2009, vol. 60, pp. 1113–16.
23. H. Kitahara, R. Ueji, N. Tsuji, and Y. Minamino: *Acta Mater.*, 2006, vol. 54, pp. 1279–88.
24. B. Li: *J. Appl. Phys.*, 2004, vol. 95, pp. 1698–1705.
25. W. Mu, P. Hedström, H. Shibata, P.G. Jönsson, and K. Nakajima: *JOM*, 2018, vol. 70, pp. 2283–95.
26. H. Yin, T. Emi, and H. Shibata: *ISIJ Int.*, 1998, vol. 38, pp. 794–801.
27. D. Phelan and R. Dippenaar: *ISIJ Int.*, 2004, vol. 44, pp. 414–21.
28. S. Morito, X. Huang, T. Furuhara, T. Maki, and N. Hansen: *Acta Mater.*, 2006, vol. 54, pp. 5323–31.
29. X. Yu, J.L. Caron, S. Babu, J.C. Lippold, D. Isheim, and D.N. Seidman: *Acta Mater.*, 2010, vol. 58, pp. 5596–5609.
30. A.J. Wilkinson and T.B. Britton: *Mater. Today*, 2012, vol. 15, pp. 366–76.
31. M. Zha, H. Zhang, Z. Yu, X. Zhang, X. Meng, H. Wang, and Q. Jiang: *J. Mater. Sci. Technol.*, 2018, vol. 34, pp. 257–64.
32. A. Hasnaoui, H. Van Swygenhoven, and P.M. Derlet: *Acta Mater.*, 2002, vol. 50, pp. 3927–39.
33. E. Ma: *Scripta Mater.*, 2003, vol. 49, pp. 663–68.
34. A. Lambert-Perlade, A.F. Gourgues, J. Besson, T. Sturel, and A. Pineau: *Metall. Mater. Trans. A*, 2004, vol. 35A, pp. 1039–53.
35. A. Lambert-Perlade, A.F. Gourgues, and A. Pineau: *Acta Mater.*, 2004, vol. 52, pp. 2337–48.
36. X.N. Peng, Y. Peng, J.S. Wei, and Z.L. Tian: *Appl. Mech. Mater.*, 2012, vol. 217, pp. 1987–93.
37. J. Moon, S.-J. Kim, and C. Lee: *Mater. Sci. Eng. A*, 2011, vol. 528, pp. 7658–62.